Experimental and numerical study of the ignition of hydrogen-air mixtures by a localized stationary hot surface

R. Mével[*,a,b], J. Melguizo-Gavilanes[c,d], L.R. Boeck[c], J.E. Shepherd[c]

[a] Center for Combustion Energy, Tsinghua University, Beijing 100084, China
[b] Department of Automotive Engineering, Tsinghua University, Beijing 100084, China
[c] Graduate Aerospace Laboratories, California Institute of Technology, Pasadena, CA, USA
[d] Institut Pprime, UPR 3346 CNRS, ISAE-ENSMA, BP 40109, 86961 Futuroscope-Chasseneuil Cedex, France

Abstract

The ignition of hydrogen-air mixtures by a stationary hot glow plug has been experimentally investigated using two-color pyrometry and interferometry. The ignition process was characterized by the surface temperature at ignition, as well as by the location where the initial flame kernel was formed. The experimental results indicate that: (i) the ignition temperature threshold is a function of equivalence ratio; (ii) the ignition location is a function of the rate at which the glow plug is heated because high heating rates favor non-uniform heating. As a result, ignition occurs on the side rather than near the top face of the glow plug. Comparison with two-dimensional numerical simulations exhibits discrepancies in terms of the temperature threshold value and dependence on equivalence ratio. Simulations performed imposing a non-uniform surface temperature show that a temperature difference between the side and the top of the glow plug as low as 12.5 to 25 K resulted in side ignition for hydrogen-air mixtures. The effect of surface chemistry was estimated numerically by imposing a boundary condition of zero species concentration for intermediate species, H and HO_2, at the hot surface , which increased the ignition threshold by up to 50 K for an initial H_2 concentration of 70 %. The present study shows that surface temperature non-uniformity, heterogeneous chemistry and reaction model used, could influence the experimentally reported and numerically predicted ignition threshold as well as the location of ignition.

*Corresponding author: mevel@mail.tsinghua.edu.cn

1. Introduction

The accidental ignition of flammable mixtures and subsequent flame propagation is a major safety concern for a number of industrial activities such as commercial aviation, chemical processes, nuclear energy production, and mining [1–3]. Heated surfaces represent a potential hazard that needs to be assessed in order to prevent and mitigate accidental combustion events. For hot surface ignition, several cases can be differentiated based on two important parameters: (i) whether the surface is stationary or moving with respect to the reactive gas; (ii) the characteristic length scale of the hot surface. Previous work has shown that, in the case of stationary hot surfaces, two ignition regimes exist, low and high temperature ignition. For extended large surfaces, low-temperature chemistry needs to be considered. This latter configuration is more relevant to hydrocarbon fuels like n-alkanes which exhibit auto-ignition temperature on the order of 500 K as reported by Colwell and Reza [4], Kuchta et al. [5] and Council [6]. For localized small surfaces, high-temperature chemistry needs to be considered. The present study focuses on a stationary localized surface with an imposed heating rate. Similar configurations were studied by Roth et al. [7, 8], Beyer and Markus [9], Dubaniewicz [10], Dubaniewicz et al. [11], Dubaniewicz et al. [3], Bothe et al. [12], Homan [13], Boettcher et al. [14], Boettcher [15], and Menon et al. [16]. These previous studies demonstrated the importance of the mixture chemical properties and surface properties (e.g. geometry, material) on the minimum surface temperature required to ignite a reactive gas.

Another important parameter for hot surface ignition is the rate at which the surface is heated. In the low-temperature regime, Boettcher et al. [17] and Melguizo-Gavilanes et al. [18] showed that the heating rate imposed on an extended hot surface determines the type of reaction that the reactive mixture experiences, namely slow oxidation or rapid explosion. For a small hot surface, Menon et al. [16] showed that for n-hexane-air mixtures, the chemical processes characteristic of the negative temperature coefficient region influence the ignition behavior. In a previous study by Mével et al. [19], the effect of the hot surface heating rate on the ignition threshold and ignition location (relative to the hot surface) was investigated,

using a commercial glow plug. It was found that for hydrogen-air mixtures, fast heating of the ignition device (~200 K/s) could modify the evolution of the reported minimum ignition temperature as a function of equivalence ratio and lead to side ignition. However, under ideal conditions, ignition should not take place at the side of the glow plug as shown by Melguizo-Gavilanes et al. [20, 21] and Boeck et al. [22]. Numerical simulations by Melguizo-Gavilanes et al. [20, 21] have predicted ignition to occur at the location where chemical runaway is favored because heat transport by conduction and mass diffusion is minimized. In addition, Boeck et al. [22] showed using a uniformly heated horizontal cylinder that, the most favorable ignition location is where the spatial temperature gradient is the shallowest, that is where the thermal boundary layer is the thickest. For the commercial glow plug employed by Mével et al., the location at which these conditions are fulfilled corresponds to the stagnation point at the top wall. Consequently, non-ideal effects such as non-homogeneous heating of the glow plug surface could influence the ignition threshold and the ignition location.

The present study investigates the effect of surface temperature non-homogeneity on the hot surface ignition threshold and ignition dynamics for hydrogen-air mixtures of different equivalence ratios. In particular, we seek to explain the mechanism whereby side ignition occurs for the specific hot surface (a commercial glow plug) we employed in several of our previous studies. To achieve this goal, we (i) performed spatially and temporally resolved measurements of surface temperature during the heating period which enabled us to validate and verify our numerical simulations, (ii) measured the thermal ignition threshold over the entire range of flammability of H_2-air mixtures which complements previous measurements done at specific concentrations, (iii) quantified the effect of temperature non-uniformity on the ignition threshold through numerical simulation using realistic profiles and parametric analyses, and (iv)performed a preliminary investigation of the effect of the species surface boundary conditions on the ignition threshold.

2. Experimental setup

2.1. Combustion vessel

The ignition experiments were performed in a closed vessel with a volume of 2.2 L. This combustion facility has been previously described in detail by Boettcher et al. [14], Boettcher [15] and Menon et al. [16]. Briefly, the vessel inner dimensions were 114 mm x 114 mm x 171 mm. Quartz windows on each side of the vessel enabled optical access, and an additional sapphire window provided access for optical temperature measurement. An electrically heated glow plug (Autolite 1110) was used as the hot surface vertical cylinder 9.3 mm in height and 5.1 mm in diameter) bounded by a horizontal plate at the bottom. The glow plug was connected to a low voltage power supply for heating and placed at the center of the bottom plate of the vessel. A pressure transducer (Heise model 901A) located on the filling line of the vessel was used to prepare the mixtures using the partial pressure method.

2.2. Surface temperature measurement

A two-color pyrometer was used to make non-contact measurements of the glow plug surface temperature by comparing the intensity of radiation emitted by the hot glow plug in 100 nm bands around two different near-infrared wavelengths, 1705 and 1940 nm. The relationship between intensities at each wavelength λ and temperature T is derived from Plank's law. For small λ, the spectral irradiance $L_\lambda(T)$ writes $L_\lambda(T) \approx \varepsilon_\lambda C_1/\lambda^5 \exp(-C_2/\lambda T)$, where ε_λ is the spectral emissivity, and C_1 and C_2 are Plank's radiation constants. The radiation intensity $I(T)$ is obtained for small bandwidths $\Delta\lambda$: $I(T) \approx \varepsilon_\lambda C_1/\lambda^5 \exp(-C_2/\lambda T)\Delta\lambda$. The relationship between the ratio of radiation intensities, I_1/I_2, at two wavelengths, λ_1 and λ_2, and temperature, T, is expressed as

$$\ln\left(\frac{I_1}{I_2}\right) = \frac{A}{T} + B \tag{1}$$

where $A = C_2(1/\lambda_2 - 1/\lambda_1)$ and $B = \ln[(\lambda_2^5 \Delta\lambda_1)/(\lambda_1^5 \Delta\lambda_2)]$.

Coefficients A and B in Equation 1 were obtained through calibration using a Process Sensors BBS1200 black body radiation source with variable aperture.

Note that Equation 1 assumes wavelength-independent emissivity. However, for the glow plug material (stainless steel 316) a difference in emissivity of up to 2.5 %, was reported by Touloukian and DeWitt [23] between the two pyrometer wavelengths used. This results in a measurement uncertainty (see Coates [24]), unless, the emissivity variation is taken into account using

$$T = \left[\frac{1}{C_2} \cdot \frac{\lambda_1 \lambda_2}{\lambda_2 - \lambda_1} \cdot \ln\left(\frac{\epsilon_1}{\epsilon_2}\right) + \frac{1}{T_m} \right]^{-1}, \tag{2}$$

where T is the real surface temperature, T_m is the measured temperature assuming wavelength-independent emissivity, and ϵ_1 and ϵ_2 are the emissivities at the wavelengths λ_1 and λ_2, respectively.

To estimate the overall systematic surface temperature measurement uncertainty, the following components were taken into account: (1) calibration uncertainty due to accuracy and stability of the calibration source (+/-0.2%); (2) effect of signal noise (+/-1%); (3) effect of variability in emissivity (see Equation 2, e.g., +0/-2.5% at 1000 K); (4) temperature difference between the location of the temperature measurement and the ignition location (+/-2.5%, s. subsection 4.1). The overall uncertainty will be shown by error bars in Figure 6 and is on the order of +3.7/-6.2%.
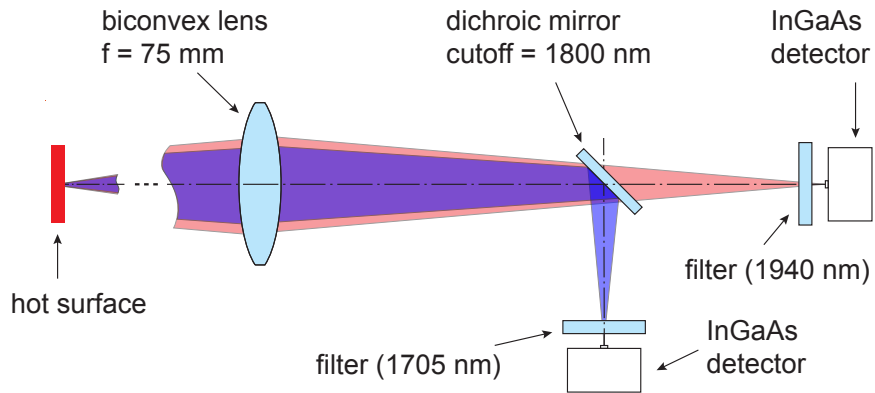

Figure 1: Schematic of the optical pyrometer layout.

In, Mével et al. [19], we found that the measurement accuracy of the ignition threshold was very sensitive to the calibration method and the optical design of the two-color pyrometer. Consequently, a new chromatic aberration-compensated

pyrometer with a small field-of-view was implemented to enable an accurate and precise local measurement of the glow plug temperature. Figure 1 shows a schematic of the improved two-color pyrometer. The light from the glow plug passes through a convex lens, a dichroic beam splitter with a cutoff wavelength of 1800 nm, and two bandpass filters. Finally, intensities are registered by two InGaAs photo detectors. Focal shift due to chromatic aberration was computed for the specific convex lens and is compensated for by different path lengths between the dichroic mirror and the respective detectors.
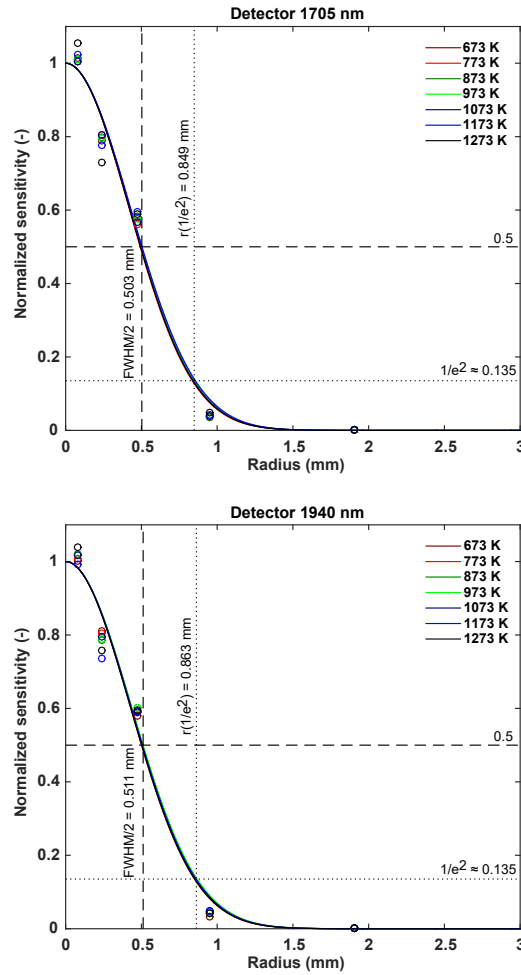

Figure 2: Measured pyrometer sensitivity profiles for the two wavelength bands examined.

Variation of the black body aperture enabled the characterization of the pyrometer field-of-view and spatial sensitivity profile. The pyrometer was focused on the

aperture center and intensities I_1 and I_2 were recorded for five black body aperture radii. Various black body temperatures were used to minimize potential effects of non-uniform emission. Each increase in aperture radius corresponded to the addition of an emitting ring area and caused an increase in intensity. Assuming spatially uniform emission from the black body surface, the discrete spatial sensitivity was defined as the intensity collected from a respective ring area, divided by the area of the ring, and assigned to the arithmetic mean of outer and inner radius of the ring. Figure 2 shows normalized sensitivity as a function of pyrometer field-of-view radius for both detectors, i.e., for both wavelength bands. Discrete sensitivities (markers) were approximated by a Gaussian (lines) with a FWHM of 1.02 mm and a $1/e^2$ diameter of 1.72 mm. Due to chromatic shift compensation, the sensitivity diameters differ by less than 1.6% between the two wavelength bands.
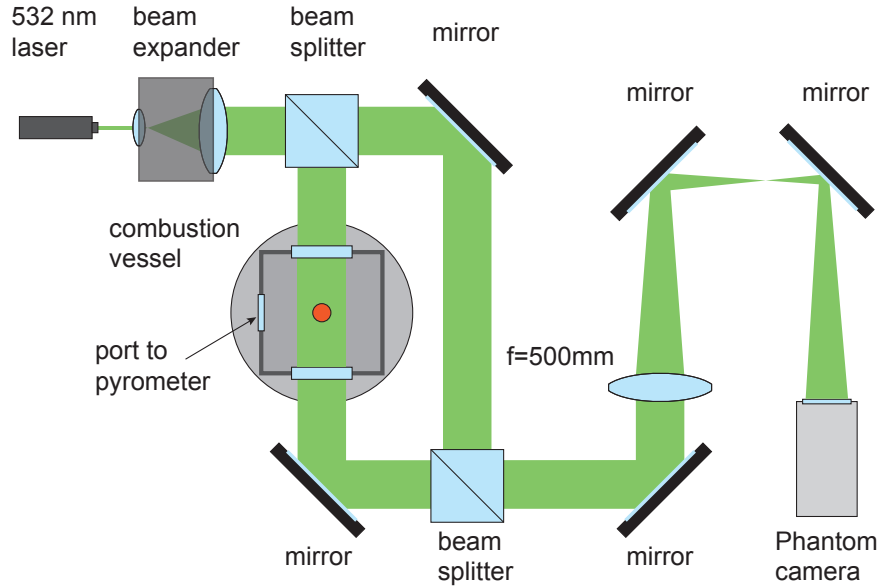

Figure 3: Schematic of the Mach-Zehnder interferometer.

2.3. Flow visualization

Figure 3 shows a schematic of the Mach-Zehnder interferometer used to visualize the gas density field in the vessel. A 532 nm solid state laser (Spectra Physics Excelsior) was used as the light source. The beam was expanded and divided by a prismatic beam splitter cube. One beam was directed through the vessel and then

turned with a mirror. The other beam (i.e. the reference beam) was also turned with a mirror and the two beams were subsequently recombined in a second prismatic beam splitter cube. A 500 mm focal length converging lens between the cubic prism and high-speed camera (Phantom V 7-11) was used to locate the camera focus in the glow plug center plane. The interferograms obtained with the Mach-Zehnder interferometer capture the optical path length difference between light traveling through the combustion vessel with refractive index $n(z)$ and a reference field with initial refractive index n_0. In the present experiment configuration, z corresponds to the axis that is normal to the vessel windows. The optical phase difference, $\Delta\varphi$, is related to the refractive index by

$$\Delta\varphi = \varphi - \varphi_0 = \frac{2\pi}{\lambda} \int_{\xi_1}^{\xi_2} \left[n(z) - n_0 \right] \mathrm{d}z, \tag{3}$$

where ξ_1 and ξ_2 are the locations along the z–axis where a ray of light enters and leaves the test section, respectively, and λ is the wavelength of the light source. The intensity, I, of a two-dimensional fringe pattern is represented by an amplitude and frequency modulated function,

$$I(x, y) = \hat{a}(x, y) + \hat{b}(x, y) \cos\left(\Delta\varphi(x, y)\right) \tag{4}$$

where $\hat{a}$ denotes the background illumination and noise, $\hat{b}$ is the amplitude, and φ is the phase, see Rastogi and Hack [25]. The phase demodulation of the interferograms, i.e. obtaining $\Delta\varphi$, is accomplished by using the 2D Windowed Fourier Filtering method (WFF2) of Kemao [26].

We did not make a detailed investigation of the temperature field in the present study. The quantitative application of interferometry to temperature measurement in ignition situations and validation are discussed in depth by Coronel et al. [27, 28].

2.4. Experimental procedure

Prior to each experiment, the vessel was evacuated to less than 10 Pa and filled with hydrogen, oxygen and nitrogen to obtain the desired mixture. The gases were then mixed using a circulation pump, and left to settle for 3 minutes. The power supply was turned on to start heating of the glow plug. Measurement systems were synchronized with the power supply. The vessel gas temperature and pressure,

and the pyrometer detector voltages were recorded using two digital recorders (Pico Technology PicoScope and LeCroy Wavesurfer 44 MXs). The Phantom V 7-11 high-speed camera was operated at 10,000 fps and triggered from the pressure increase during the combustion event.

3. Numerical methodology

3.1. Governing equations

The motion, transport and chemical reaction in the gas surrounding the glow plug were modeled using the variable-density reactive Navier-Stokes equations with temperature-dependent transport properties. Differential diffusion effects were taken into account using a constant but non-unity Lewis number for each species, Le_i, as proposed by Poinsot and Veynante [29]. The form that the heat and mass diffusion fluxes take when written as a function of Le_i can be found in Melguizo-Gavilanes et al. [20] along with all the computational methodology, spatial and temporal discretization details, and models used to account for the functional temperature dependence of mixture viscosity, thermal conductivity and specific heat. Thermodiffusion (Soret effect) and radiation were neglected. The governing equations were solved in an axisymmetric two dimensional geometry using the Open source Field Operation And Manipulation (OpenFOAM) toolbox (Weller et al. [30]). Our implementation of the code has been validated in various ignition studies comprising different geometries, modes of heat transfer (e.g. forced and natural convection), and ignition timescales, see Melguizo-Gavilanes et al. [20, 21, 31, 32], Jones et al. [33], Melguizo-Gavilanes et al. [18], and Mével et al. [34], respectively.

3.2. Chemical kinetic mechanisms

The chemistry was modeled using Mével et al. [35, 36], Hong et al. [37], Konnov [38], and GRI-Mech 3.0 [39] reaction models. These detailed mechanisms for hydrogen oxidation include for the H_2-O_2-diluent system 11 species and 42, 40, 37, and 36 reactions, respectively. In the 11 species mentioned, Ar and N_2 are included as diluents. In addition, the sub-model of Mével et al. [35] for excited OH* radicals was added to each model because the time to OH* peak was used as our ignition

criterion for the adiabatic constant pressure 0-D simulations. It accounts for 9 of the total reaction number given above. Although all mechanism were validated against extensive kinetics databases, they show significantly different behaviors (see subsection 5.1 for a detailed discussion).

3.3. Domain, initial and boundary conditions

The geometry simulated closely corresponded to that described in section 2. The rectangular prism used in the experiments was approximated by a cylindrical vessel of radius 114 mm and height 171 mm with a glow plug of 9.3 mm x 5.1 mm located at (0,0). There were 200,000 cells in the 2D-axisymmetric computational domain, compressed near the wall of the glow plug, with a minimum cell size of $80\,\mu$m to resolve the thermal and hydrodynamic boundary layers.

The initial conditions were $P_o = 101\,$kPa, $T_o = 300\,$K, $U_o = (0,0)\,$m/s, and mass fractions Y_{H_2}, Y_{O_2}, Y_{N_2}, corresponding to a hydrogen mole fraction ranging from 10% to 70%. No-slip boundary condition and constant temperature $T_{wall} = T_o$ were imposed on the vessel walls. On the glow plug surface, a prescribed temperature ramp given by $T(t) = T_o + rt$ with $r = 220\,$K/s was used. This heating rate is higher than the one used in the experiments (55 - 65 K/s). For heating rates in this range, we have previously shown [20] through experiment and numerical simulation that the effect on ignition threshold is modest varying at most by 25 K for heating rates between 18 and 190 K/s. Only for extremely slow heating rates, corresponding to large surfaces and longer residence times [17] is heating rate expected to be a significant factor. Finally, the boundary conditions for species were set to either zero flux or zero concentration to assess the effect of surface reactions.

4. Experimental results

4.1. Characterization of the glow plug surface temperature during heating

To characterize the glow plug surface temperature during the heating process, scanning pyrometry was employed. This approach is similar to that previously used by Boeck et al. [22] for studying ignition of hydrogen-, ethylene-, and n-hexane-air
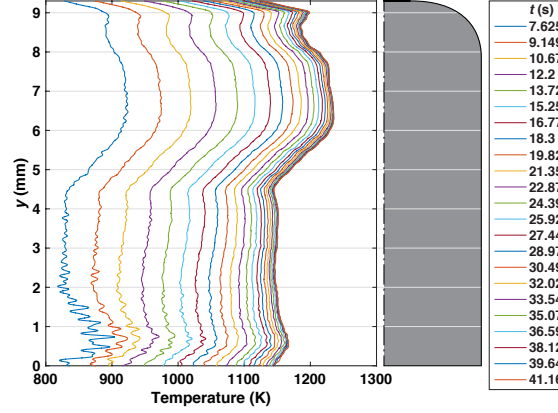
Figure 4: Glow plug surface temperature profiles obtained from scanning pyrometry in air for a heating between 298 and 1000 K at an average rate of 65 K/s. Profiles represent averages between consecutive bidirectional scans.

mixtures by a vertical/horizontal hot cylinder. The two-color pyrometer field-of-view was translated vertically at a rate of 6.35 mm/s along the glow plug side between the stagnation plate and the glow plug tip, using a translation stage motorized by a stepper motor. This resulted in duration of each scan of about 1.5 s. In order to minimize the effect of transient heating on the measurement, we performed pair-wise averaging of consecutive scans. For the present heating rate, the error arising from the assumption of piece-wise linear heating between consecutive scans is smaller than +/- 3 K at all times during the heating process, and diminishes towards the end where a steady-state temperature profile is approached.

Figure 4 presents temperature profiles at times between 7.6 and 41.2 s after the beginning of heating in air. Since the glow plug is heated internally by a coiled wire located in the upper section, a distinct temperature peak is observed at heights above the stagnation plate, y, between 6 and 8 mm. Since the temperature scans are convoluted with the Gaussian pyrometer sensitivity profile, readings in regions below 1.5 mm and above 7.8 mm cannot be interpreted. In the current setup the glow plug temperature at the time of ignition can only be measured at the side of the glow plug. For the ignition experiments, we positioned the pyrometer field-of-view at the location of maximum temperature ($6 < y < 8$). However, ignition preferentially occurs at the glow plug top as will be shown later. To assess the difference in temperature

between the top and side of the glow plug measurement location, we performed additional pyrometer scans of the top and compared against the peak temperatures on the side at corresponding times. This revealed a slightly lower temperature at the top compared to the side with a maximum difference of 2.5% (25 K). This difference is accounted for as part of the measurement uncertainty for the ignition threshold, see subsection 2.2.
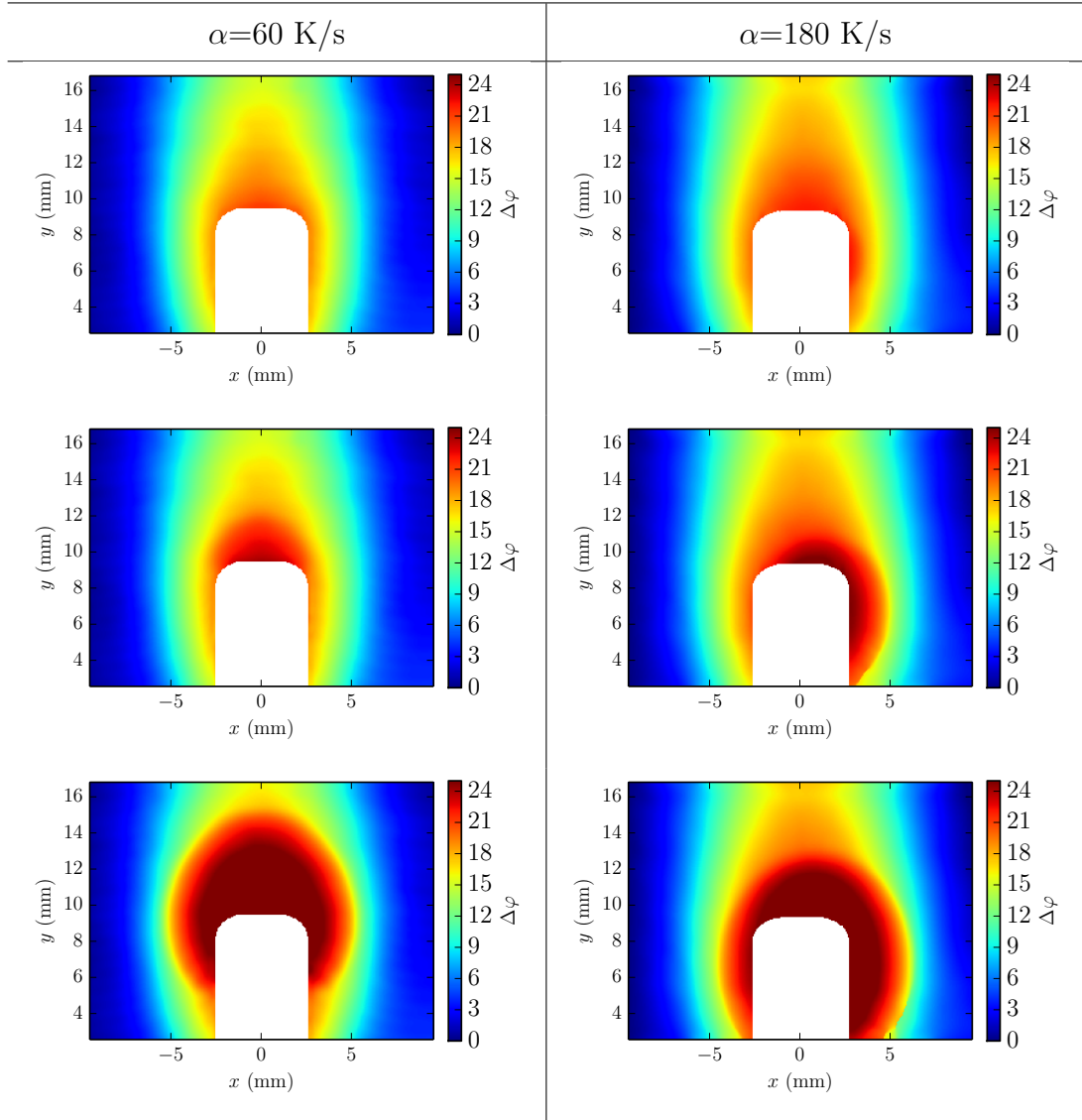

Figure 5: Optical phase difference $\Delta\varphi$ fields illustrating the effect of the heating rate on the ignition location. Conditions: stoichiometric hydrogen-air; P=101 kPa; $T_o = 300$ K; Heating rate 60 K/s with top ignition (left) and 180 K/s with side ignition (right).

13

Figure 5 shows time-resolved experimental optical phase difference fields of the ignition process. Line-of-sight integrated phase difference from interferometry is reported rather than temperature since the latter can only be obtained in the case of axisymmetric ignition events. For a moderate heating rate, 60 K/s (left column), ignition occurs just above the top of the glow plug on the symmetry axis. At higher heating rates, 180 K/s, ignition is observed to occur on the side of the glow plug (right column). This asymmetry was previously attributed by Mével et al. [19] to inhomogeneous glow plug surface temperature at high heating rates. Rapid heating increases the uncertainty of the ignition threshold measurements since the location of ignition is random and possibly has a different temperature than the area monitored with the pyrometer. As a result, a moderate heating rate of 55-65 K/s was chosen to determine the ignition thresholds shown in Figure 6.
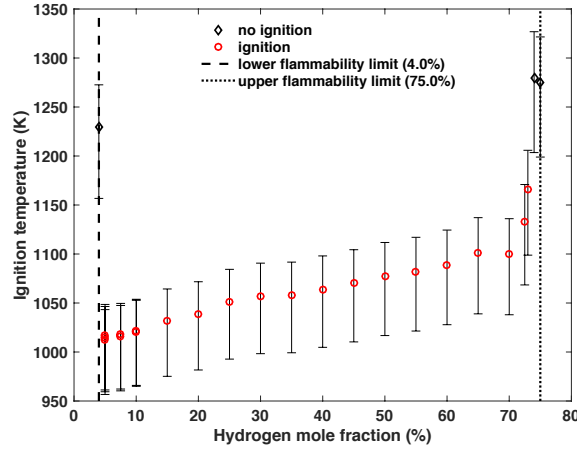

Figure 6: Evolution of the ignition temperature threshold as a function of hydrogen mole fraction for hydrogen-air mixtures. Conditions: P=101 kPa, and $T_o = 300$ K. Lower (LFL) and upper (UFL) flammability limits are shown as dashed and dotted vertical lines, respectively. Error bars indicate temperature measurement uncertainty, see subsection 2.2.

Figure 6 shows the variation of the ignition threshold as a function of hydrogen mole fraction. The reported temperatures are the peak temperatures on the side of the glow plug at the time of ignition, measured with the stationary pyrometer at a height y of 6-8 mm (see Fig. 4). For the no-ignition cases, the highest surface

temperature reached after a heating time of 60 s is reported. Ignition thresholds increase from lean to rich mixtures, ranging between 1010 K and 1100 K with an additional increase to 1170 K close to the upper flammability limit. For all hydrogen mole fractions tested, ignition took place symmetrically above the top of the glow plug. The variability in ignition threshold between repeated tests was much smaller, on the order of 0.2%, in comparison to the measurement uncertainties, which are on the order of +3.7/-6.2%. For example, three tests at a hydrogen concentration of 5% resulted in ignition thresholds of 1012 K, 1017 K and 1015 K.

5. Numerical results

5.1. Reaction model selection

Hot surface ignition is the result of competition between reaction and and diffusive transport of species and thermal energy. Using 1-D numerical simulations, Coronel [40] showed, using an impulsively heated hot plate, that the ignition delay-time is increased up to 50% as compared to 0-D calculations. The importance of radical diffusion on the ignition threshold for moving hot spheres was also emphasized by Melguizo-Gavilanes et al. [32]. Acknowledging that the effects of diffusion are important, we have separately investigated the influence of the choice of reaction rates and mechanism by carrying out a series of zero-dimensional, adiabatic induction time computations with various mechanisms. These calculations are very rapid and can be used to quickly explore differences between reaction mechanisms.

A large number of reaction models are available to describe the combustion of hydrogen-oxygen mixtures, see Olm et al. [41]. The predictions and accuracy of these models differ strongly depending on the parameter of interest as shown by Chaumeix et al. [42], Mével et al. [43], and Olm et al. [41]. In the present study, eight models were considered: Mével et al. [35, 36], Hong et al. [37], Konnov [38], GRI-Mech 3.0 [39], JetSurf [44], CaltechMech [45], Ó Conaire et al. [46], and Le Cong [47]. Figure 7 shows the predictions of the eight reaction models for 0-D adiabatic constant pressure simulations for a stoichiometric hydrogen-air mixture at P=101
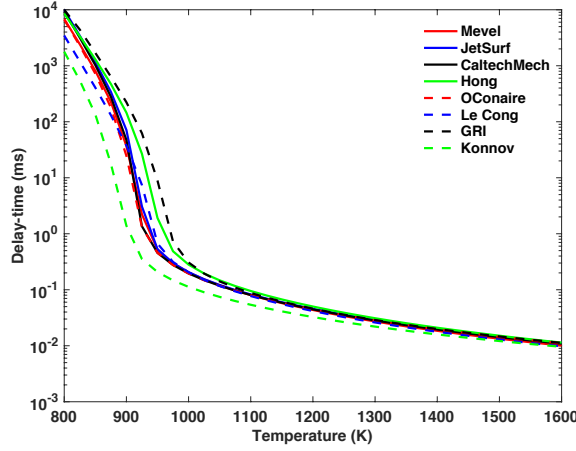
Figure 7: Evolution of the constant pressure (P=101 kPa) ignition delay-time of a stoichiometric hydrogen-air mixture as a function of temperature for eight reaction models.

kPa. The ignition delay-time was defined as the time to maximum OH concentration.

While the reaction models predictions are consistent in the high-temperature range, very large differences are seen at temperatures below 1000 K. For example, at 900 K, GRI-Mech predicts an ignition delay-time 160 times longer than Konnov's mechanism. To investigate further the effect of reaction model on the ignition threshold, four models were selected: (i) the GRI-Mech, which predicts the longest delay-time, (ii) Konnov's model, which predicts the shortest delay-time, (iii) Mevel's model, which predicts intermediate delay-time, and (iv) Hong's model, whose predictions are the most sensitive to equivalence ratio. This aspect is illustrated in Figure 8 which shows the evolution of the delay time as a function of temperature for mixtures with different hydrogen concentrations. The temperature at which an abrupt change of activation energy (cross-over temperature between low- and high-temperature chemistry) is predicted to increase by about 50 K between the mixtures containing 10% and 70% of H_2 by the model of Hong et al. whereas for the other models, this increase is predicted to be of 10 to 20 K. The difference in prediction between the different models can mainly be explained by the value of the rate constant used for the reaction $H+O_2(+M)=HO_2(+M)$.
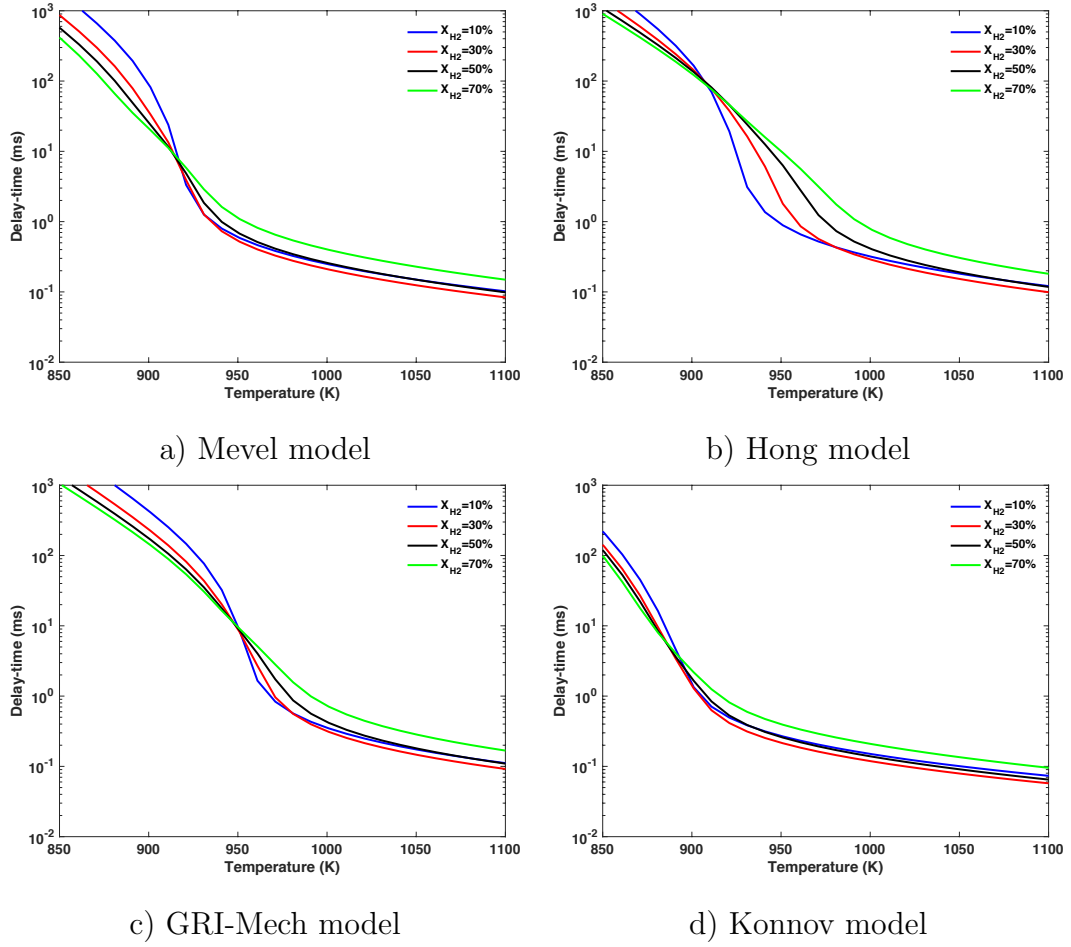
16

a) Mevel model   b) Hong model

c) GRI-Mech model   d) Konnov model

Figure 8: Evolution of the constant pressure (P=101 kPa) ignition delay-time of hydrogen-air mixtures as a function of temperature and hydrogen concentration for four reaction models.

5.2. 2-D fields during ignition

5.2.1. Uniform heating

A detailed analysis of the ignition dynamics for the present geometry was performed in Melguizo-Gavilanes et al. [20] to identify important flow features such as thermal and hydrodynamic boundary layers, flow separation, thermal plume temperature, velocity distributions, chemical activity and ignition location. Here we show the typical ignition evolution predicted for a uniformly heated surface, and use it to support a later discussion on the effect of the temperature non-uniformities present experimentally during the heating of the glow plug. Two-dimensional fields of temperature and velocity (magnitude), velocity vectors, and mass fractions of OH and HO_2 are shown in Figure 9 and Figure 10. Three different times, t=τ_{ign}-375 μs (shortly before ignition), t=τ_{ign}=2.899875 s (ignition kernel formation), and t=τ_{ign}+75 μs (early stages of flame propagation) show the ignition evolution. All fields are re-scaled to cover their full range within the computational domain at each time.

Figure 9 (top) shows the temperature and velocity (magnitude) fields obtained at t=τ_{ign}-375 μs of heating along with velocity vectors showing the buoyancy flow induced by the glow plug. The velocity vectors illustrate the flow occurring near and above the glow plug. In the vicinity of the hot surface there is a thermal boundary layer and above the glow plug, a thermal plume. Fresh cold gas enters the thermal boundary layer from below and heats up as it travels upward along the side of the glow plug surface. The thermal boundary layer separates once the gas reaches the upper edge of the glow plug, creating a region at the top of the hot surface where the gas stagnates. Outside of this region, the mixture continues to rise to the top of the combustion vessel. Figure 10 (top) shows that chemical activity is confined to the top of the glow plug from very early on, where the temperature gradient normal to the surface is shallowest because convective losses are minimal. The temperature maximum in the domain (T = 938 K) corresponds to that of the glow plug surface at this time.

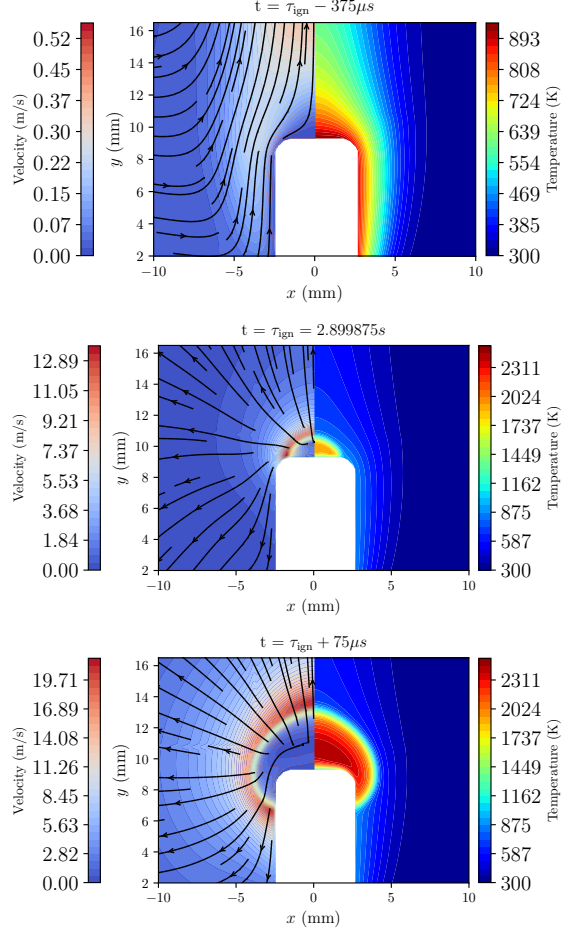At t=τ_{ign}=2.899875 s, ignition takes place. The energy release rate is sufficiently

18

Figure 9: Temperature and velocity (magnitude) fields, and velocity vectors in the vicinity of the uniformly heated glow plug for a stoichiometric hydrogen-air mixture at P=101 kPa, and T_o=300 K. At t=τ_{ign}-375 μs (shortly before ignition); at t=τ_{ign}2.899875 s (ignition kernel formation); at t=τ_{ign}-75 μs (early stages of flame propagation) using Mével's mechanism.
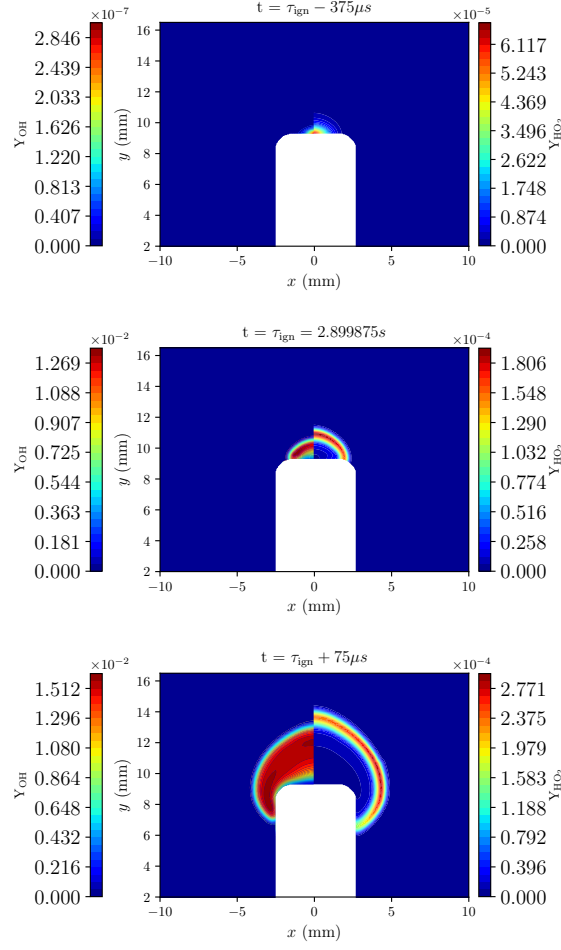
Figure 10: Species mass fraction fields (HO_2 and OH) in the vicinity of the uniformly heated glow plug for a stoichiometric hydrogen-air mixture at P=101 kPa, and $T_o = 300$ K. At t=τ_{ign}-375 μs (shortly before ignition); at t=τ_{ign}=2.899875 s (ignition kernel formation); at t=τ_{ign}+75 μs (early stages of flame propagation) using Mével's mechanism.

strong to overcome diffusive and convective losses, raising the temperature to 1960 K. The high reactivity of stoichiometric hydrogen-air mixtures is evidenced by the strong acceleration of the gas ahead of the ignition kernel with a velocity increase from 0.674 to 13.8 m/s over 375 μs (see Figure 9 – center). The mass fraction of OH peaks across the flame front (see Figure 10), whereas that of HO_2 peaks in the pre-heat zone ahead of the flame as expected. The last frame in Figure 9, at t=τ_{ign}+75 μs, shows the early stages of flame propagation. The gas continues to accelerate from 13.8 to 21.2 m/s in an even shorter time interval with the maximum in velocity located immediately ahead of the flame. The shape of the flame is determined by the preferential propagation of the combustion front along the thermal plume where fresh combustible mixture is hottest.

From the evolution shown above, a combustible mixture exposed to a uniformly heated glow plug should always ignite at the top where the interaction of the flow with the hot surface creates the critical conditions for ignition to occur. In this region, as explained above, convective losses are minimal resulting in a shallow temperature gradient and higher temperatures further away from the wall allowing for the chemical source term to increase exponentially [20]. The side ignition observed experimentally should then be caused by a temperature difference between the side and the top of the glow plug induced by non-uniform heating at high heating rates. To test this hypothesis, a temporally and spatially varying boundary condition was imposed on the glow plug surface and the results are discussed next.

5.2.2. Non-uniform heating

Additional simulations were run in which the boundary condition for temperature on the surface of the glow plug was given by $T(t,y) = [T_o + A\sin(\pi y/h)] + \alpha t$ (see Figure 11). This corresponds to half of a sine wave with amplitude A that peaks at $y = h/2$ where $h = 9.3$ mm is the height of the glow plug. We could have used/imposed the same profile as that shown in Figure 4, however the current choice enables to easily change the amplitude of the non-uniformity to systematically study how the

temperature difference between the top and the side of the glow plug influences the ignition behavior and location. We recognize that the current approach corresponds to a simplification of the experimental configuration since the temperature difference between the top and the side of the glow plug is likely time-dependent and here, we modeled it as constant.
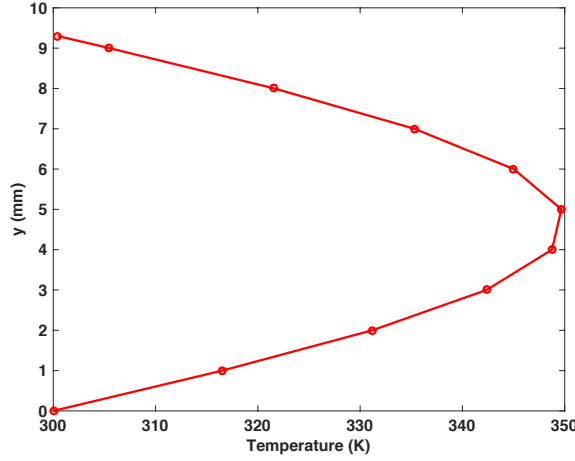

Figure 11: Initial temperature distribution imposed on the glow plug surface given by $T(t,y) = (T_o + A\sin(\pi y/h)]) + \alpha t$ where A is the amplitude of the sine wave, y is the vertical coordinate along the glow plug surface and h is the height of the glow plug; α is the previously defined heating rate.

A temperature difference of 50 K on the surface of the glow plug was sufficient to trigger side ignitions. Two additional values of A were tested (25 and 12.5 K) to determine the minimum value of A that will no longer result in side ignitions. A temperature difference of 25 K also resulted in an ignition kernel forming on the side of the glow plug. However for A=12.5 K, ignition took place at the top. No further values of A were considered, hence it can be concluded that for stoichiometric hydrogen-air mixtures, non-uniformities in the range 12.5–25 K are required to trigger side ignitions. In the discussion section we will explain, using chemical kinetic arguments, why hydrogen-air mixtures are particularly sensitive to temperature non-uniformities. This is in contrast with mid-size hydrocarbons like n-hexane that exhibit more stable behavior experimentally even when high temperature ramps (~ 220 K/s) are used, see Boettcher [15].
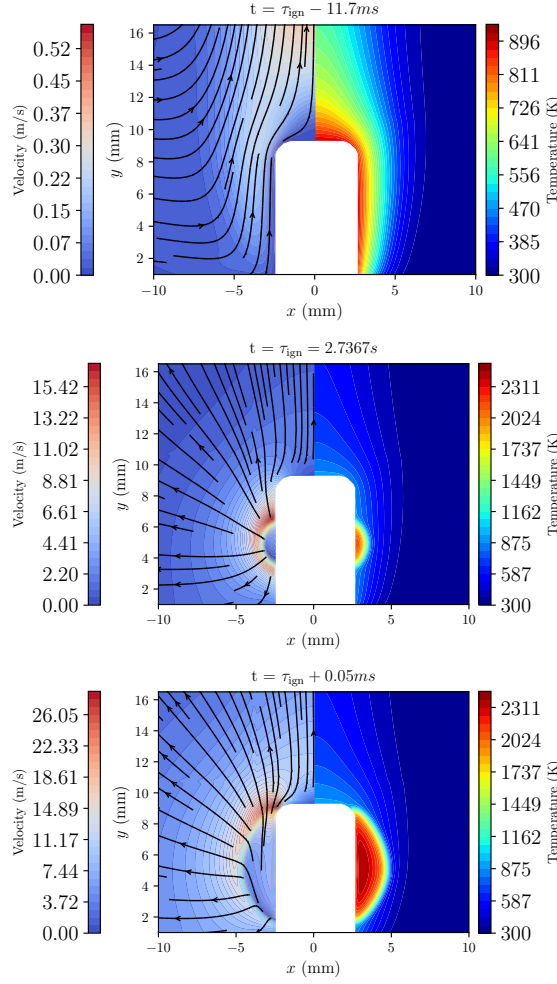
Figure 12: Temperature and velocity (magnitude) fields, and velocity vectors in the vicinity of the non-uniformly heated glow plug for a stoichiometric hydrogen-air mixture at P=101 kPa, and T_o=300 K. At t=τ_{ign}-11.7 ms (early stages of heating); at t=τ_{ign}=2.7367 s (ignition kernel formation); at t=τ_{ign}+0.05 ms (early stages of flame propagation) using Mével's mechanism.
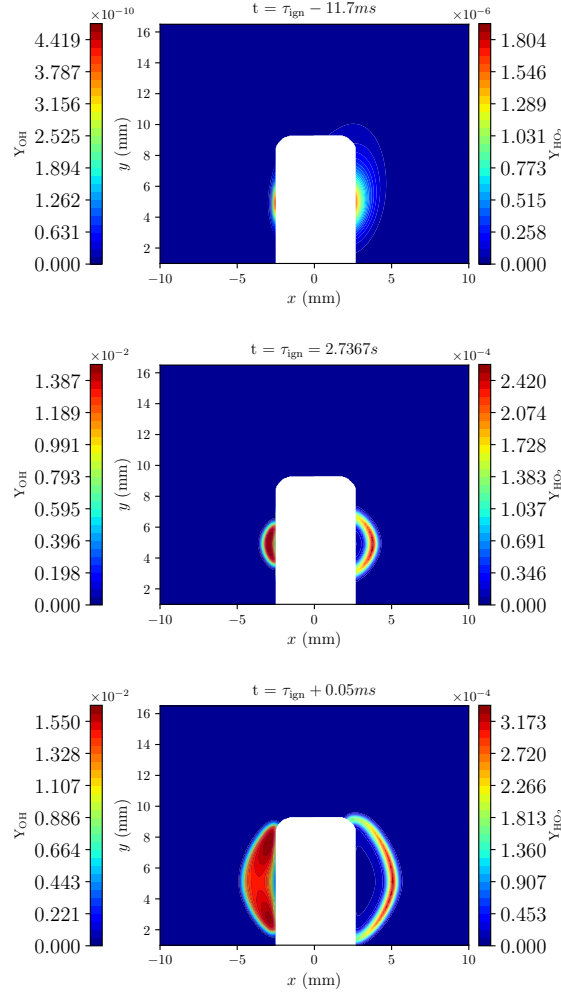
Figure 13: Species mass fraction fields (HO_2 and OH) in the vicinity of the non-uniformly heated glow plug for a stoichiometric hydrogen-air mixture at P=101 kPa, and $T_o = 300$ K. At t=τ_{ign}-11.7 ms (early stages of heating); at t=τ_{ign}=2.7367 s (ignition kernel formation); at t=τ_{ign}+0.05 ms (early stages of flame propagation) using Mével's mechanism.

Figure 12 and Figure 13 show the same fields presented for the uniform heating case but with A=50 K. Note that at t=τ_{ign}-11.7 ms, temperature and velocity fields are virtually unaffected by the presence of the temperature non-uniformity imposed on the glow plug wall, and visually, are close to those shown in Figure 9. Experimentally the same outcome is observed (see Figure 5 top row). Because a fluid parcel traveling along the side of the glow plug will experience higher temperatures close to the wall than for the uniform heating case, the mass fraction fields show that chemical activity is no longer located at the top of the glow plug but at the side. Shortly after, an ignition kernel appears, and subsequent flame propagation takes place.

5.3. Effect of hydrogen concentration on the ignition temperature threshold

Twenty-four additional simulations were performed to construct Figure 14 which shows the effect of hydrogen concentration on the ignition threshold for the 4 kinetic mechanisms considered (6 points per model) and how they compare with the experimentally reported thresholds. The differences between the experimental and the predicted ignition thresholds range between 50 and 110 K for X_{H2}=10% and between 120 and 180 K for X_{H2}=70%. In line with the 0-D predictions shown in subsection 5.1, Konnov yields the lowest ignition threshold (910 K for X_{H2}=10% - 920 K for X_{H2}=70%), and GRI-Mech the highest (970 K for X_{H2}=10% - 980 K for X_{H2}=70%). Mével's and Hong's mechanisms lie within these bounds. However Hong's is the most sensitive to hydrogen concentration yielding ignition thresholds of 948 K for X_{H2}=10% - 970 K for X_{H2}=70%, whereas Mével's exhibits no dependence as a function of hydrogen concentration with an essentially flat ignition threshold of 938 K.

To gain insight into the differences between the reaction models predictions, we examined the temporal species profiles at the ignition location predicted by Mevel's and Hong's models for 10% and 70% H_2 in air. These are shown in Figure 15. For the 10% H_2 case, the ignition temperature predicted by the two models is close (938
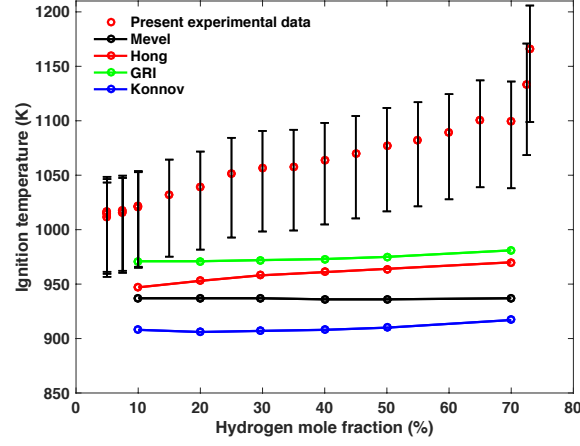
Figure 14: Effect of mixture concentration on the numerically predicted (2-D) ignition threshold for hydrogen-air mixtures using four different kinetic mechanisms. Conditions: P=101 kPa, and $T_o = 300$ K.
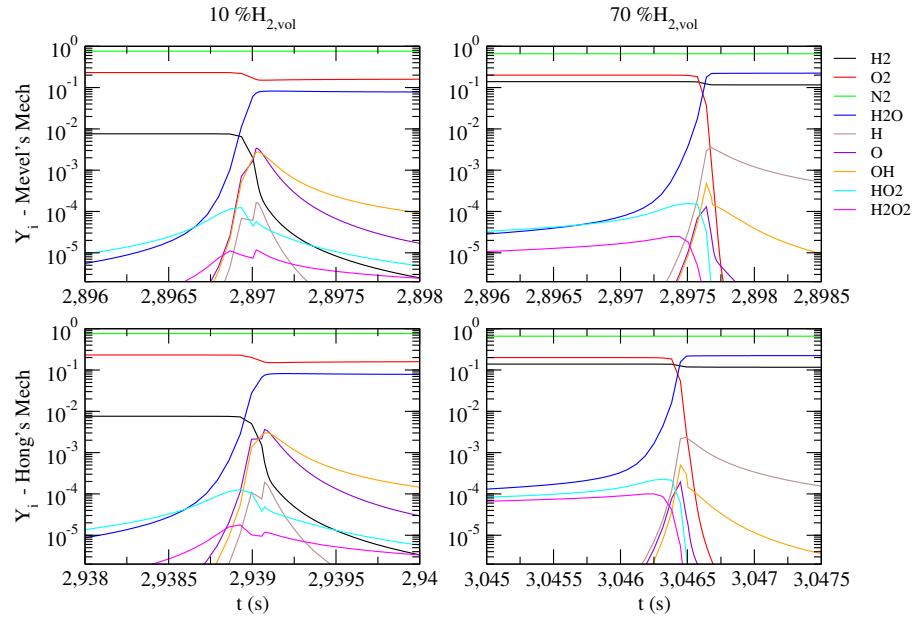

Figure 15: Species mass fraction profiles at the ignition location predicted by Mevel's and Hong's models for hot surface ignition of hydrogen-air mixtures with 10% and 70% H_2. Conditions: P=101 kPa, and $T_o = 300$ K.

K for Mevel and 948 K for Hong) and the profiles for most species are quasi-identical in shape and amplitude. The most noticeable difference is observed for H_2O_2 whose mass fraction exceeds 10^{-6} 0.5 ms earlier for the simulation performed with Hong's model. For the 70% H_2 case, the ignition threshold is 938 K for Mevel's model and 970 K for Hong's model. Although the species profiles for the major species are very similar, more pronounced differences are observed for HO_2 and H_2O_2 with predicted mass fractions respectively three and six times higher at 1.5 ms prior to ignition for the simulation performed with Hong's model. In addition, the ratio Y_{HO2}/Y_{H2O2} is higher for the simulation performed with Hong's model. The difference of ignition threshold between the two reaction models is then mainly explained by the higher thermal stability of HO_2 and H_2O_2 predicted by Hong's model. Because of this higher stability, the production of active radicals (OH) from these two species is delayed for the simulation performed with Hong's model resulting in a higher ignition threshold.

5.4. Effect of surface reaction on the ignition temperature threshold

While the numerical simulations also predict an increase in threshold with increasing hydrogen concentration when the model of Hong et al. is used, the predicted ignition threshold is quantitatively lower than that found experimentally by 70 K for X_{H2}=10 % and 130 K for X_{H2}=70 % (see Figure 14). We speculate that because of the reactivity of the glow plug surface (316 stainless steel), the ignition threshold may be increased due to surface chemistry. Based on the previous experimental evidence [7, 9], the ignition thresholds obtained with chemically active materials tend to be higher than for a non-reactive surface. This increase is attributed to the enhanced recombination of reactive radicals at the surface, see Roth et al. [7]. As demonstrated by Glorian et al. [48, 49] and Maestri and Cuoci [50], numerical modeling of surface reactions requires significant code development as well as careful estimation of the rates of the physical and chemical processes taking place, and is therefore beyond the scope of the present study. Nevertheless, it is possible to obtain an upper limit of the effect of species quenching/adsorption at the wall of the glow plug by changing the boundary condition for the species of interest from von Neumann (zero gradient) to Dirichlet (fixed value). A similar approach was used

by Sano and Yamashita [51] to investigate the ignition of methane-air flames within a thermal boundary layer. We chose to set the value of the mass fractions of H (most diffusive species) and HO_2 (important species according to an ignition pathway analysis performed in Melguizo-Gavilanes et al. [20]) to zero independently, and then allow both to vanish simultaneously, to assess their effect on the numerically predicted ignition threshold. This exercise was carried out using Hong's mechanism only as this kinetic scheme shows the strongest dependence with hydrogen concentration among the mechanisms considered.
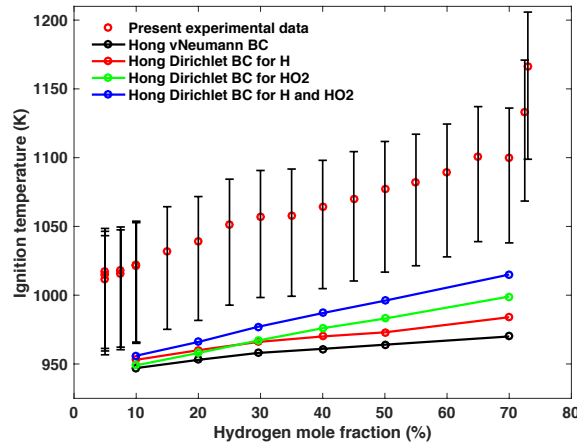

Figure 16: Effect of species quenching at glow plug surface on the numerically predicted (2-D) ignition threshold for hydrogen-air mixtures of different concentrations using Hong's mechanism. Conditions: P=101 kPa, and T_o = 300 K. vNeumann BC corresponds to the reference case.

Figure 16 shows the results. Destruction of H atoms at the wall brings the ignition threshold up to 985 K for X_{H2}=70 %. HO_2 has a greater influence with a numerical threshold of 1000 K for X_{H2}=70 %. Setting both intermediate species mass fractions to zero at the wall results in an ignition threshold of 955 K for X_{H2}=10 % and 1015 K for X_{H2}=70 %. With this approach, the predicted thresholds are 65 and 85 K lower than those found experimentally, respectively for X_{H2}=10 and 70 %. These latest numerical results are to be taken with caution, and were included here merely to show what behavior is to be expected when species are quenched at the wall, and how this affects the numerically predicted ignition thresholds. Implementation of heterogeneous chemistry in our numerical model will be a topic of future work.

6. Discussion

Figure 17 summarizes the experimental and numerical results of the present study along with the experimental results from Kumar [52], Roth et al. [7, 8], and Beyer and Markus [9]. Our experimental results place the surface temperature threshold for ignition of hydrogen-air mixtures at 1010, 1050 and 1100 K for X_{H2}=5, 30 and 70 %, respectively. According to Kumar [52], the ignition threshold lies at about 930 K and is independent of the hydrogen content between 10 and 50% of hydrogen in air. Direct comparison of our experiments with Kumar's results is not possible due to the difference between the two experimental configurations. Kumar employed a closed vessel and heated the mixtures with four slowly heated (5 K/s) stainless steel rods. The fluid motion was very different than in the present experiments which could significantly influence the ignition temperature threshold, as well as the much lower heating rate. In addition, the temperature was measured using thermocouples strapped to the hot surfaces which, according to our previous results (see Mével et al. [19]) could significantly underestimate the surface temperature. Issues with thermocouple temperature measurements in this type of flows include conduction losses along the leads, temperature gradients in the boundary layer, thermal contact resistance between hot surface and thermocouple, and convective and radiative heat losses from the thermocouple and leads to the surroundings. Based on our previous results, surface temperatures measured using contact thermocouples could be up to 150 K lower than the actual surface temperature for temperatures on the order of 1000 K. Consistent values were reported by Smyth and Bryner [53].

Experimental configurations closer to the present study include Roth et al. [7, 8] and Beyer and Markus [9] who investigated the ignition of hydrogen-air mixtures by laser heated spherical particles. Roth et al. [7] investigated a large number of experimental configurations by varying both the sphere diameter and the surface material. To maintain the clarity of the discussion, we have selected a few number of conditions to illustrate the main trends observed experimentally. For completeness, we included a summary of all the experimental data from the present study and from Roth et al. [7, 8], Kumar [52], and Beyer and Markus [9] as an appendix.
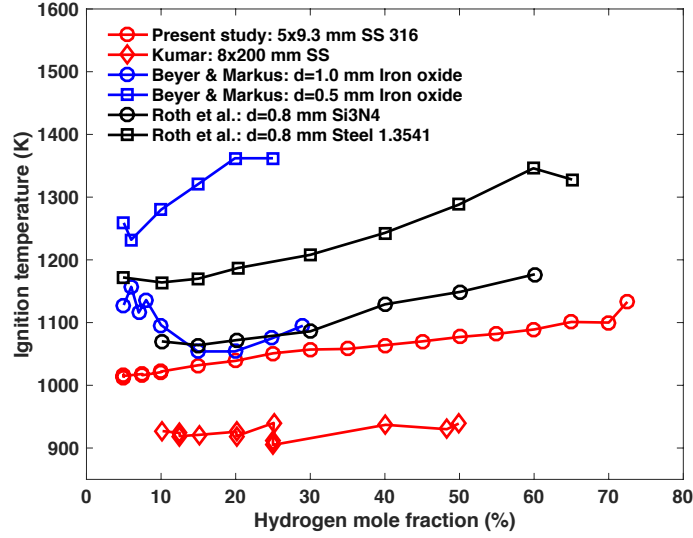
Figure 17: Summary of results: present experiments and selected literature data. Conditions: P=101 kPa, and T_o = 300 K.

Roth et al. [7], looked at the effect of material on ignition thresholds by keeping the sphere diameter fixed at 0.8 mm. Two of the materials used were Si_3N_4 (inert) and steel 1.3541 (reactive). For Si_3N_4, they reported ignition thresholds in the range 1070–1180 K, respectively for X_{H2}=10 and 60% at ambient temperature and pressure. For reactive steel spheres, they observed an increase in the ignition threshold, reporting values of 1170 K for X_{H2}=5% and 1330 K for X_{H2}=65%. These results are consistent with those from the most recent study of Roth et al. [8] performed with 0.8 mm in diameter Si_3N_4 spheres. Beyer and Markus [9] investigated the effect of particle size by using inert iron oxide spheres of 0.5 to 1 mm in diameter. The experiments were performed at 325 K and atmospheric pressure for mixtures containing between 5 and 30% of hydrogen in air. For the smallest spheres, they reported an ignition threshold between 1260 and 1360 K for X_{H2}=5 and 30 %, respectively. For the largest spheres, the reported threshold demonstrates a more complex evolution with hydrogen content; the ignition temperature first drops from 1130 K at X_{H2}=5 % to about 1050 K at X_{H2}=15 %, and then increases up to 1100 K at X_{H2}=30 %. For Roth et al. [7, 8] and Beyer and Markus [9], the reported uncertainties are on the order of ±5 %, comparable to our experiments. While most studies tend to indicate a linear increase of the threshold with hydrogen mole fraction, the uncertainty of the experimental data complicates the interpretation of this trend. Using a 1-D radial

model, Beyer and Markus [9] investigated the effect of the particle size further and found an ignition threshold independent of the diameter for spheres larger than 5 mm and a strongly increasing threshold for diameters below 1 mm. The results of Roth et al. [7, 8] and Beyer and Markus [9] seem consistent with the present experimental observations in terms of ignition threshold variations with hydrogen content, hot surface size and material, despite the very different heating rates used: 60 K/s in the present study; 360 K/s by Beyer; and 3000 K/s by Roth. The large differences between the heating rates used in these studies could, however, result in significant discrepancies in the nature of the flow induced. For a heating rate of 3000 K/s, Roth et al. [8] concluded that the ignition process was controlled by chemical kinetics rather than by transport. Because under our experimental configuration and that of Beyer and Markus [9], ignition takes place at a location where convection losses are minimized, transport phenomena control the ignition location rather than the ignition threshold. Our numerical simulations indicate that the ignition event should preferentially occur at the top of the glow plug slightly above the surface. As explained in subsection 5.2, flow separation at the top edge of the glow plug, results in the formation of an essentially stagnant pocket of gas above the top of the glow plug resulting in longer residence times hence thermal runaway is more likely to occur. Under conditions where non-uniform heating of our specific ignition device surface occurs, both experimental and numerical results demonstrate that ignition can take place on the side of the glow plug. This outcome is supported by the very large activation energy of the auto-ignition process for hydrogen-air mixtures in the temperature range of interest 900–1000 K. The sensitivity of the delay-time to temperature is on the order of -1.2 to -8.5 %/K. This results in a delay-time up to 25 times shorter for a temperature difference of 20 K. Consequently, the parcel of gas that travels along the side of the glow plug can ignite before the volume of gas stagnating just above the top surface of the glow plug. For hydrocarbon fuels such as n-hexane, the temperature sensitivity of the ignition delay-time for temperatures close to the ignition threshold (1200–1300 K) is only of about -0.5 %/K. As a result, a much larger temperature non-uniformity would be required to induce side ignition for these fuels.

From the above analysis of the present results and those from the literature, it is noted that the ignition by hot surface is a very complex process which depends on residence time of the gas in the vicinity of the hot surface, the surface area, the material properties, and the chemical behavior of the reactive mixture. All these contributing aspects make the reported ignition temperature specific to the particular configuration employed during the experiments. Because the ignition thresholds do not strictly apply to different situations, they do not constitute absolute values and should be considered with caution. For H_2-air mixtures, ignition was observed for temperatures above 1000 K in all the studies except that of Kumar who used a much larger hot surface. These results demonstrate the predominant importance of the surface area and associated residence time since ignition was observed by Kumar at temperatures on the order of 900 K despite the dramatic increase of the ignition delay-time below 950 K. In this regime of temperature, an increased importance of the low-temperature chemical pathways, responsible for the formation of peroxides, is observed [20]. The ignition process is further complicated by the diffusion of the intermediates to the wall and their reaction at the surface which may promote (decomposition reaction: H_2O_2=2OH) or inhibit (recombination reaction: OH+H=H_2O) chemical run-away, depending on the specific chemical activity of the material.

7. Conclusion

The hot surface ignition of hydrogen-air mixtures was characterized in terms of ignition temperature threshold and ignition location using electrically heated commercial glow plug. The dynamics of the ignition process was characterized using a two-color pyrometer calibrated with a black body radiation source and high-speed visualization based on the Mach-Zehnder interferometry technique. The effects of composition and temperature non-uniformities on the glow plug were investigated experimentally and numerically. The experimental ignition threshold demonstrated an increase from 1010 K for X_{H2}=5 % to 1170 K for X_{H2}=74 %, close to the upper flammability limit. The present results demonstrate consistent trends with previous

32

experimental studies. The heating rate was found to influence the ignition location with high heating rates favoring ignition on the side of the glow plug whereas moderate heating rates resulted in ignition just above the top surface of the glow plug. Two-dimensional numerical simulations were performed for both uniform and non-uniform hot surfaces. The predicted ignition temperature threshold were found to be lower than the experimental measurements by 40 to 180 K, depending on the reaction model used in the simulations. Only the mechanism of Hong et al. [37] reproduced the increase in threshold with hydrogen concentration observed experimentally. The effect of surface chemistry was investigated in a very approximate fashion by setting the concentration of H and HO_2 to zero at the glowplug surface and determining the effect on ignition threshold. This resulted in an increase of the ignition threshold of up to 50 K for X_{H2}=70 %. These results are consistent with our previous reaction pathway analyses (Melguizo-Gavilanes et al. [20]) of the ignition of hydrogen-air mixtures by a hot surface which demonstrated the importance of H and HO_2 for the ignition process through the sequence: $H+O_2(+M)=HO_2(+M)$; $HO_2+H=OH+OH$. It was also shown that, due to the very high activation energy of the ignition process for hydrogen-air mixtures in the temperature range of 900-1000 K, a temperature difference between the side and the top of the glow plug as low as 12.5-25 K could cause side ignition. The present results indicate that hot surfaces with well defined properties are needed to enable a precise characterization of the ignition process in terms of temperature threshold and ignition dynamics. In order to make a direct comparison with the numerical simulations, surface reactions should be accounted for in the simulations but this approach requires significant code development and accurate estimation of the surface reaction kinetics.

Acknowledgments

Appendix: Summary of ignition temperature threshold data

The available data on the ignition temperature of hydrogen-air mixtures by a stationary hot surface are summarized in Figure 18 and Table 1 to Table 5.

Table 1: Present ignition temperature measurements for hydrogen-air mixtures using a commercial glow plug made of stainless steel 316.

Dimension (mm)	X_{H2} (%)	T_{ig} (K)	Material
5 x 9.3	5.0	1012	SS 316
5 x 9.3	5.0	1017	SS 316
5 x 9.3	5.0	1015	SS 316
5 x 9.3	7.5	1018	SS 316
5 x 9.3	7.5	1016	SS 316
5 x 9.3	10.0	1021	SS 316
5 x 9.3	10.0	1022	SS 316
5 x 9.3	15.0	1032	SS 316
5 x 9.3	20.0	1039	SS 316
5 x 9.3	25.0	1051	SS 316
5 x 9.3	30.0	1057	SS 316
5 x 9.3	35.0	1058	SS 316
5 x 9.3	40.0	1064	SS 316
5 x 9.3	45.0	1070	SS 316
5 x 9.3	50.0	1077	SS 316
5 x 9.3	55.0	1082	SS 316
5 x 9.3	60.0	1089	SS 316
5 x 9.3	65.0	1101	SS 316
5 x 9.3	70.0	1100	SS 316
5 x 9.3	72.5	1133	SS 316
5 x 9.3	73.0	1166	SS 316

Table 2: Ignition temperature measurements by Kumar [52] for hydrogen-air mixtures using stainless steel heated rods.

Dimension (mm)	X_{H2} (%)	T_{ig} (K)	Material
8 x 200	10.2	927	SS
8 x 200	12.5	924	SS
8 x 200	12.5	919	SS
8 x 200	15.1	921	SS
8 x 200	20.1	926	SS
8 x 200	20.1	919	SS
8 x 200	25.1	940	SS
8 x 200	25.0	911	SS
8 x 200	25.0	905	SS
8 x 200	40.1	937	SS
8 x 200	48.3	930	SS
8 x 200	49.9	939	SS

Table 3: Ignition temperature measurements by Beyer and Markus [9] for hydrogen-air mixtures using a spherical particle.

Diameter (mm)	X_{H2} (%)	T_{ig} (K)	Material
1	5.0	1128	Iron oxide
1	6.0	1157	Iron oxide
1	7.0	1116	Iron oxide
1	8.0	1136	Iron oxide
1	10.0	1096	Iron oxide
1	14.9	1054	Iron oxide
1	19.9	1054	Iron oxide
1	24.9	1075	Iron oxide
1	29.0	1095	Iron oxide
0.75	6.0	1205	Iron oxide
0.75	7.0	1205	Iron oxide
0.75	8.0	1280	Iron oxide
0.75	10.0	1259	Iron oxide
0.75	14.9	1162	Iron oxide
0.75	20.0	1280	Iron oxide
0.75	24.9	1300	Iron oxide
0.5	5.0	1259	Iron oxide
0.5	6.0	1232	Iron oxide
0.5	10.0	1280	Iron oxide
0.5	15.0	1321	Iron oxide
0.5	19.9	1362	Iron oxide
0.5	25.0	1362	Iron oxide

Table 4: Ignition temperature measurements by Roth et al. [8] for hydrogen-air mixtures using a spherical particle.

Diameter (mm)	X_{H2} (%)	T_{ig} (K)	Material
0.8	4.9	1163	Si_3N_4
0.8	9.9	1081	Si_3N_4
0.8	15.0	1075	Si_3N_4
0.8	20.0	1085	Si_3N_4
0.8	30.7	1085	Si_3N_4
0.8	46.9	1132	Si_3N_4
0.8	53.4	1156	Si_3N_4
0.8	61.0	1176	Si_3N_4

Table 5: Ignition temperature measurements by Roth et al. [7] for hydrogen-air mixtures using a spherical particle.

Diameter (mm)	X_{H2} (%)	T_{ig} (K)	Material
0.3	5.1	1291	Tungsten
0.3	10.1	1320	Tungsten
0.3	15.0	1285	Tungsten
0.3	20.1	1256	Tungsten
0.3	30.0	1278	Tungsten
0.8	5.1	1074	Tungsten
0.8	10.1	1072	Tungsten
0.8	15.0	1082	Tungsten
0.8	20.1	1082	Tungsten
0.8	30.2	1116	Tungsten
0.8	40.0	1100	Tungsten
0.8	49.9	1183	Tungsten
0.8	60.1	1210	Tungsten
0.6	4.9	1113	Steel 1.3505
0.6	9.9	1111	Steel 1.3505
0.6	15.0	1088	Steel 1.3505
0.6	19.9	1123	Steel 1.3505
0.6	30.0	1155	Steel 1.3505
0.6	40.0	1176	Steel 1.3505
0.6	50.1	1233	Steel 1.3505
0.8	4.9	1066	Steel 1.3505
0.8	10.1	1064	Steel 1.3505
0.8	15.0	1060	Steel 1.3505
0.8	19.9	1086	Steel 1.3505
0.8	30.0	1115	Steel 1.3505

Diameter (mm)	X_{H2} (%)	T_{ig} (K)	Material
0.8	40.0	1147	Steel 1.3505
0.5	15.0	1133	Si_3N_4
0.5	19.9	1131	Si_3N_4
0.5	50.1	1222	Si_3N_4
0.8	10.1	1070	Si_3N_4
0.8	15.0	1064	Si_3N_4
0.8	20.1	1072	Si_3N_4
0.8	30.0	1086	Si_3N_4
0.8	40.0	1129	Si_3N_4
0.8	50.1	1149	Si_3N_4
0.8	60.1	1177	Si_3N_4
0.4	4.9	1319	Steel 1.4034
0.4	10.1	1305	Steel 1.4034
0.4	15.0	1311	Steel 1.4034
0.4	19.9	1317	Steel 1.4034
0.4	30.0	1350	Steel 1.4034
0.4	40.0	1412	Steel 1.4034
0.5	4.9	1282	Steel 1.4034
0.5	10.1	1272	Steel 1.4034
0.5	15.0	1265	Steel 1.4034
0.5	19.9	1292	Steel 1.4034
0.5	30.0	1332	Steel 1.4034
0.5	40.0	1363	Steel 1.4034
0.5	49.9	1410	Steel 1.4034
0.7	5.3	1168	Steel 1.4034
0.7	9.9	1170	Steel 1.4034
0.7	15.0	1172	Steel 1.4034
0.7	20.1	1156	Steel 1.4034

| Diameter (mm)	X_{H2} (%)	T_{ig} (K)	Material
0.7	30.0	1179	Steel 1.4034
0.7	40.0	1191	Steel 1.4034
0.7	50.1	1249	Steel 1.4034
0.7	60.1	1317	Steel 1.4034
0.6	5.1	1197	Steel 1.3541
0.6	10.1	1195	Steel 1.3541
0.6	15.0	1212	Steel 1.3541
0.6	20.1	1205	Steel 1.3541
0.6	30.2	1234	Steel 1.3541
0.6	40.0	1265	Steel 1.3541
0.6	50.1	1276	Steel 1.3541
0.8	4.9	1172	Steel 1.3541
0.8	10.1	1164	Steel 1.3541
0.8	15.0	1170	Steel 1.3541
0.8	20.3	1187	Steel 1.3541
0.8	30.0	1208	Steel 1.3541
0.8	40.0	1243	Steel 1.3541
0.8	49.9	1288	Steel 1.3541
0.8	59.9	1346	Steel 1.3541
0.8	65.1	1328	Steel 1.3541
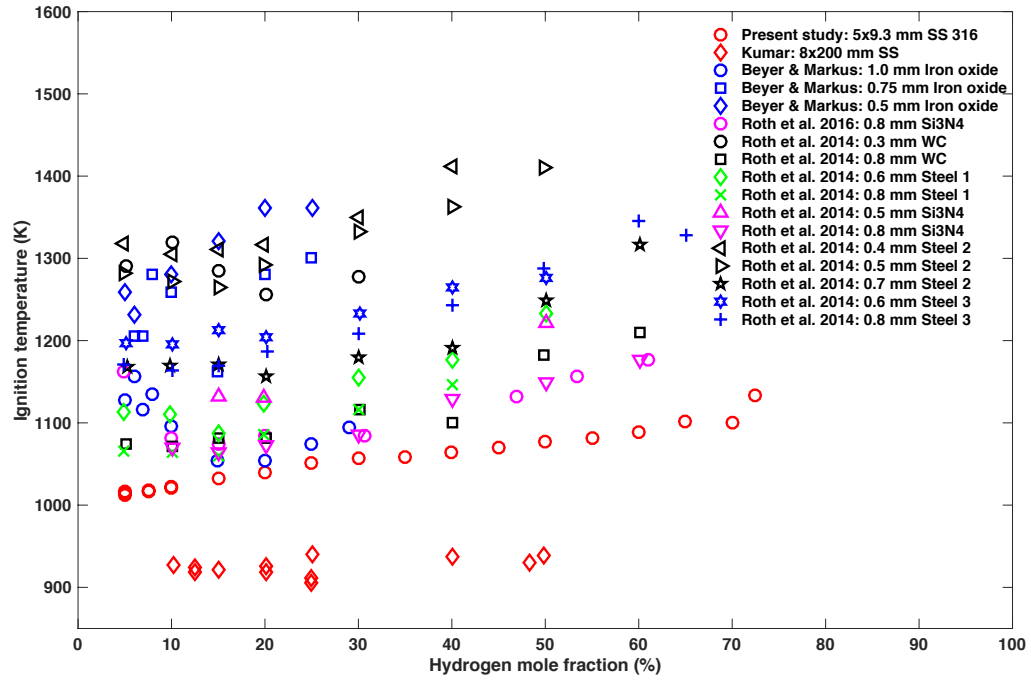
Figure 18: Summary of available data on stationary hot surface ignition of hydrogen-air mixtures from Kumar [52], Roth et al. [7, 8]. Steel 1: steel 1.3505; Steel 2: steel 1.4034; Steel 3: steel 1.3541.

References

[1] M. Burns, W. Cavage, R. Morrison, S. S., Evaluation of Fuel Tank Flammability and the FAA Inerting System on the NASA 747 SCA, Technical Report DOT/FAA/Ar-04/41, FAA, 2004.

[2] S. Dorofeev, V. Sidorov, A. Dvoinishnikov, Combustion and Flame 104 (1996) 95–110.

[3] T. H. Dubaniewicz, K. L. Cashdollar, G. M. Green, R. F. Chaiken, Journal of Loss Prevention in the Process Industries 13 (2000) 349–359.

[4] J. Colwell, A. Reza, Fire Technology 41 (2005) 105–123.

[5] J. M. Kuchta, A. Bartkowiak, M. G. Zabetakis, Journal of Chemical and Engineering Data 10 (1965) 282–288.

[6] C. R. Council, Handbook of Aviation Fuel Properties - CRC Report No. 530, Society of Automotive Engineers, Warrendale, PA, 1983.

[7] D. Roth, P. Sharma, T. Haeber, R. Schiessl, H. Bockhorn, U. Maas, Combustion Science and Technology 186 (2014) 1606–1617.

[8] D. Roth, T. Harber, H. Bockhorn, Proceedings of the Combustion Institute 36 (2017) 1475–1484.

[9] M. Beyer, D. Markus, Science and Technology of Energetic Materials 73 (2012) 1–7.

[10] T. H. Dubaniewicz, Journal of Laser Applications 18 (2006) 312–319.

[11] T. H. Dubaniewicz, K. L. Cashdollar, G. M. Green, Journal of Laser Applications 15 (2003) 184–191.

[12] H. Bothe, S. Schenk, S. Hawksworth, F. Carleton, F. Weinberg, in: Explosion Safety in Hazardous Areas, 1999. International Conference on (Conf. Publ. No. 469), pp. 44–49.

[13] H. S. Homan, Proceedings of the Symposium (International) on Combustion 18 (1981) 1709–1717.

[14] P. Boettcher, S. Menon, B. Ventura, G. Blanquart, J. Shepherd, Journal of Fluid Mechanics 735 (2013) 176–202.

[15] P. Boettcher, Thermal Ignition, Ph.D. thesis, California Institute of Technology, 2012.

[16] S. Menon, P. Boettcher, B. Ventura, G. Blanquart, Combustion and Flame 163 (2016) 42–53.

[17] P. A. Boettcher, R. Mével, V. Thomas, J. E. Shepherd, Fuel 96 (2012) 392–403.

[18] J. Melguizo-Gavilanes, P. Boettcher, A. Gagliardi, V. Thomas, R. Mével, Proceedings of the 9th Joint US Sections Meeting of the Combustion Institute, 2015 (2015).

[19] R. Mével, M.-G. J., L. Boeck, A. Nové-Josserand, Y. Kishita, S. Coronel, J. Shepherd, Proceedings of the International Symposium on Hazards, Prevention, and Mitigation of Industrial Explosions 11 (2016).

[20] J. Melguizo-Gavilanes, L. Boeck, R. Mével, J. Shepherd, International Journal of Hydrogen Energy (2016).

[21] J. Melguizo-Gavilanes, A. Nové-Josserand, S. Coronel, R. Mével, J. Shepherd, Combustion Science and Technology 188 (2016) 2060–2076.

[22] L. Boeck, M. Meijers, A. Kink, R. Mével, J. Shepherd, Combustion and Flame 185 (2017) 265–277.

[23] Y. Touloukian, D. DeWitt, Thermal radiative properties: metallic elements and alloys. IFI, Plenum, New York, 1970.

[24] P. Coates, Metrologia 17 (1981) 103.

[25] P. Rastogi, E. Hack (Eds.), Phase Estimation in Optical Interferometry, CRC Press, 2015.

[26] Q. Kemao, Appl. Opt. 43 (2004) 2695–2702.

[27] S. Coronel, J. Melguizo-Gavilanes, J. Shepherd, Experimental Fluid and Thermal Science 90 (2018) 76–83.

[28] S. Coronel, J. Melguizo-Gavilanes, R. Mevel, J. Shepherd, Combustion and Flame 192 (2018) 495–506.

[29] T. Poinsot, D. Veynante, Theoretical and Numerical Combustion, Edwards, 2005.

[30] H. Weller, G. Tabor, H. Jasak, C. Fureby, Journal of Computational Physics 12 (1998) 620–631.

[31] J. Melguizo-Gavilanes, S. Coronel, R. Mével, J. Shepherd, International Journal of Hydrogen Energy (2016).

[32] J. Melguizo-Gavilanes, R. Mével, S. Coronel, J. Shepherd, Proceedings of the Combustion Institute (2016).

[33] S. Jones, J. Melguizo-Gavilanes, J. Shepherd, Proceedings of the Combustion Institute (2018).

[34] R. Mével, U. Niedzielska, J. Melguizo-Gavilanes, S. Coronel, J. Shepherd, Combustion Science and Technology 188 (2016) 2267–2283.

[35] R. Mével, S. Javoy, F. Lafosse, N. Chaumeix, G. Dupré, C. E. Paillard, Proceedings of The Combustion Institute 32 (2009) 359–366.

[36] R. Mével, S. Javoy, G. Dupré, Proceedings of The Combustion Institute 33 (2011) 485–492.

[37] Z. Hong, D. Davidson, R. Hanson, Combustion and Flame 158 (2011) 633–644.

[38] A. Konnov, Detailed reaction mechanism for small hydrocarbons combustion. release 0.5., 2000.

[39] G. Smith, D. Golden, M. Frenklach, N. Moriarty, B. Eiteneer, M. Goldenberg, C. Bowman, R. Hanson, S. Song, W. Gardiner, V. Lissianski, Z. Qin, Gri-mech release 3.0, 2000.

[40] S. Coronel, Thermal ignition using moving hot particles, Ph.D. thesis, California Institute of Technology, 2016.

[41] C. Olm, I. Zsély, P. R., T. Varga, T. Nagy, H. Curran, T. Turányi, Combustion and Flame 161 (2014) 2219 – 2234.

[42] N. Chaumeix, S. Pichon, F. Lafosse, C.-E. Paillard, International Journal of Hydrogen Energy 32 (2007) 2216–2226.

[43] R. Mével, J. Sabard, J. Lei, N. Chaumeix, International Journal of Hydrogen Energy 41 (2016) 6905–6916.

[44] H. Wang, E. Dames, B. Sirjean, D. Sheen, R. Tangko, A. Violi, J. Lai, F. Egolfopoulos, D. Davidson, R. Hanson, C. Bowman, C. Law, W. Tsang, N. Cernansky, D. L. Miller, R. Lindstedt, A high-temperature chemical kinetic model of n-alkane (up to n-dodecane), cyclohexane, and methyl-, ethyl-, n-propyl and n-butyl-cyclohexane oxidation at high temperatures, jetsurf version 2.0, september 19, 2010 (http://melchior.usc.edu/jetsurf/jetsurf2.0)., 2010.

[45] G. Blanquart, P. Pepiot-Desjardins, H. Pitsch, Combustion and Flame 156 (2009) 588–607.

[46] M. Ó Conaire, H. Curran, J. Simmie, W. Pitz, C. Westbrook, International Journal of Chemical Kinetics 36 (2004) 603–622.

[47] T. Le Cong, Etude expérimentale et modélisation de la cinétique de combustion de combustibles gazeux : Méthane, gaz naturel et mélanges contenant de l'hydrogène, du monoxyde de carbone, du dioxyde de carbone et de l'eau, Ph.D. thesis, Université d'Orléans, 2007.

[48] J. Glorian, S. Gallier, L. Catoire, Combustion and Flame 168 (2016) 378 – 392.

[49] J. Glorian, L. Catoire, S. Gallier, N. Cesco, Proceedings of the Combustion Institute 35 (2015) 2439 – 2446.

[50] M. Maestri, A. Cuoci, Chemical Engineering Science 96 (2013) 106–117.

[51] T. Sano, A. Yamashita, JSME International Journal Series B 37 (1994) 180–186.

[52] R. Kumar, Combustion and Flame 75 (1989) 197–215.

[53] K. Smyth, N. Bryner, Combustion Science and Technology 126 (1997) 225–253.